Supplementary Information

Nano-vault architecture mitigates stress in silicon-based anodes for lithium-ion batteries

Marta Haro[1,2*], Pawan Kumar[1], Junlei Zhao[3,4], Panagiotis Koutsogiannis[1], Alexander James Porkovich[1], Zakaria Ziadi[1], Theodoros Bouloumis[1], Vidyadhar Singh[5], Emilio J. Juarez-Perez[2,7], Evropi Toulkeridou[6], Kai Nordlund[3], Flyura Djurabekova[3], Mukhles Sowwan[1], Panagiotis Grammatikopoulos[1,8*]

[1]Nanoparticles by Design Unit, Okinawa Institute of Science and Technology (OIST) Graduate University, 1919-1 Tancha, Onna-son, Okinawa 904-0495, Japan

[2]Instituto de Nanociencia y Materiales de Aragón (INMA), CSIC-Universidad de Zaragoza, Zaragoza 50009, Spain

[3]Department of Physics and Helsinki Institute of Physics, University of Helsinki, P.O. Box 43, FI-00014 Helsinki, Finland

[4]Department of Electrical and Electronic Engineering, Southern University of Science and Technology (SUSTech), 1088 Xueyuan Avenue, Shenzhen 518055, P.R. China

[5]Department of Physics, Jai Prakash University, Chapra-841301, Bihar, India

[6]Okinawa Institute of Science and Technology (OIST) Graduate University, 1919-1 Tancha, Onna-son, Okinawa 904-0495, Japan

[7]Aragonese Foundation for Research & Development (ARAID), Government of Aragon, Zaragoza 50018, Spain

[8]Particle Technology Laboratory, Institute of Process Engineering, Department of Mechanical and Process Engineering, ETH Zürich, Sonneggstrasse 3, CH-8092 Zürich, Switzerland

E-mail: mharo@unizar.es

E-mail: pgrammatikopoulos@oist.jp

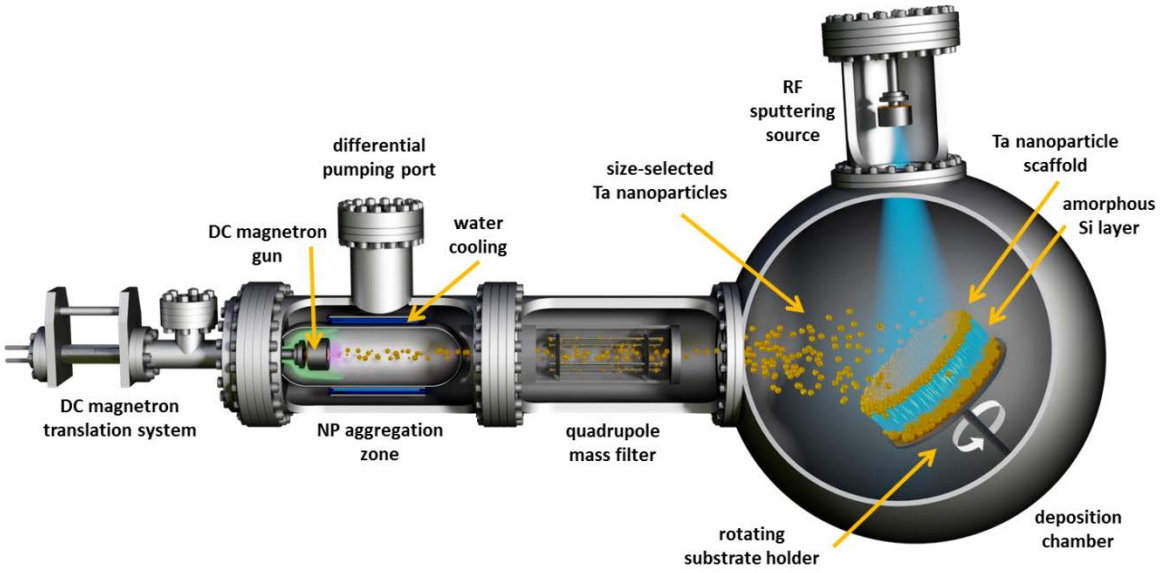

Fig. 1 | Schematic representation of the experimental setup. A sequential deposition of multiple layers of Ta nanoparticle scaffolds (by magnetron-sputtering inert-gas condensation) and overlaid amorphous Si films (by RF-sputtering) resulted in a layered configuration. *Created by Pavel Puchenkov using Blender2.8;* www.blender.org

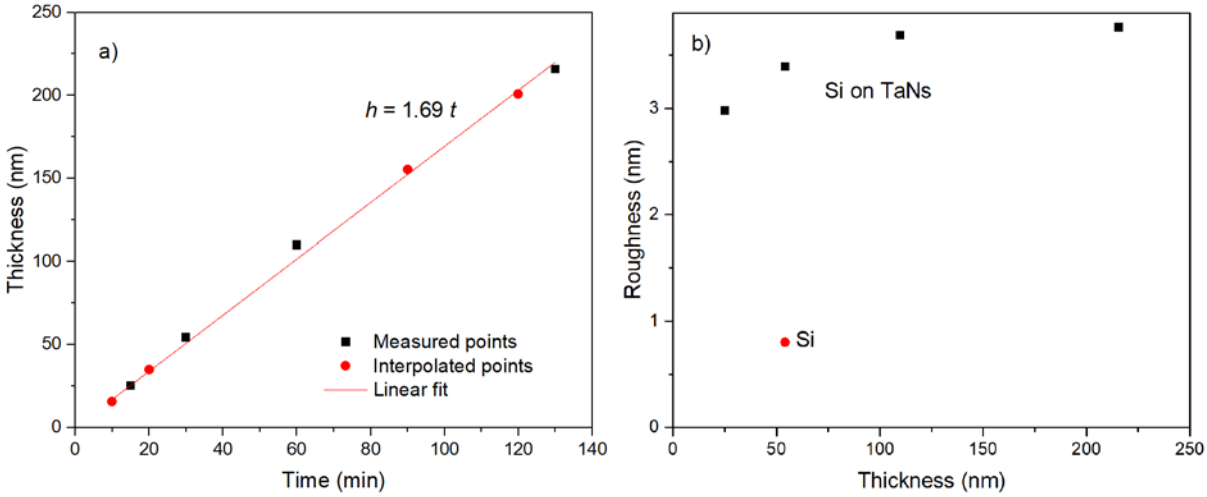

Fig. 2 | Thickness and roughness of Si films deposited on TaNS measured with XRR, for which data and experimental details are provided in Supplementary Fig. 3. a, Si film thickness (*h*) as a function of sputtering time (*t*). Black points are measured data and red points indicate interpolated thicknesses at different times. The thickness vs time points conform to the provided linear function. **b,** Roughness of deposited Si films with different thicknesses.

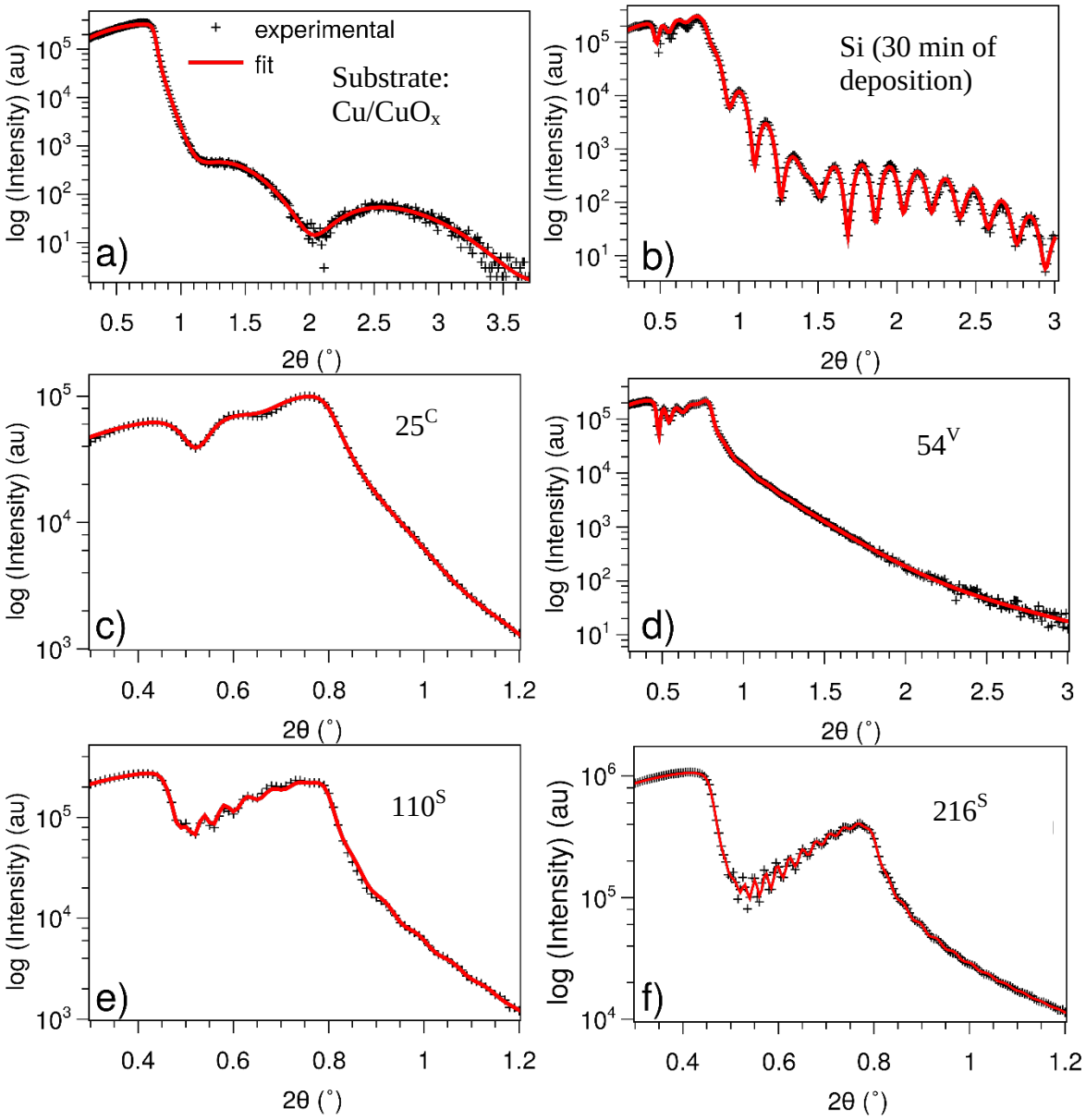

Fig. 3 | X-ray reflectivity (XRR) measurements of selected samples. The substrate employed for these measurements was Cu (100). XRR measurements were carried out using a Bruker D8 Discover instrument (Bruker AXS GmbH, Karlsruhe, Germany) equipped with Cu wavelength λ = 1.54 Å X-ray source operated at 1600 W and employing a Göbel mirror. For XRR, the beam was reduced in the reflectivity plane using a 0.05-mm slit in order to minimize the irradiated footprint at the sample position. After careful alignment of the sample, data were collected from 0.2 to 3° (2θ) with a 0.01° step. Experimental XRR data were fitted using GenX 2.4.10 software (v.2.4.10, http://genx.sf.net). **a,** A plain Cu wafer surface is modelled, including a native copper oxide layer, **b,** Si film growth without pre-deposited Ta nanoparticles show reflection fringes for 2θ > 0.8° that are absent for **d,** Si film growth on substrates with Ta nanoparticles. Thus, those fringes belong to a very flat Cu/Si interface that is absent upon deposited Ta nanoparticles. Silicon in panel b and d used the same Si deposition times. Panels **c, d, e,** and **f,** correspond to Si thin-film samples using different Si deposition times.

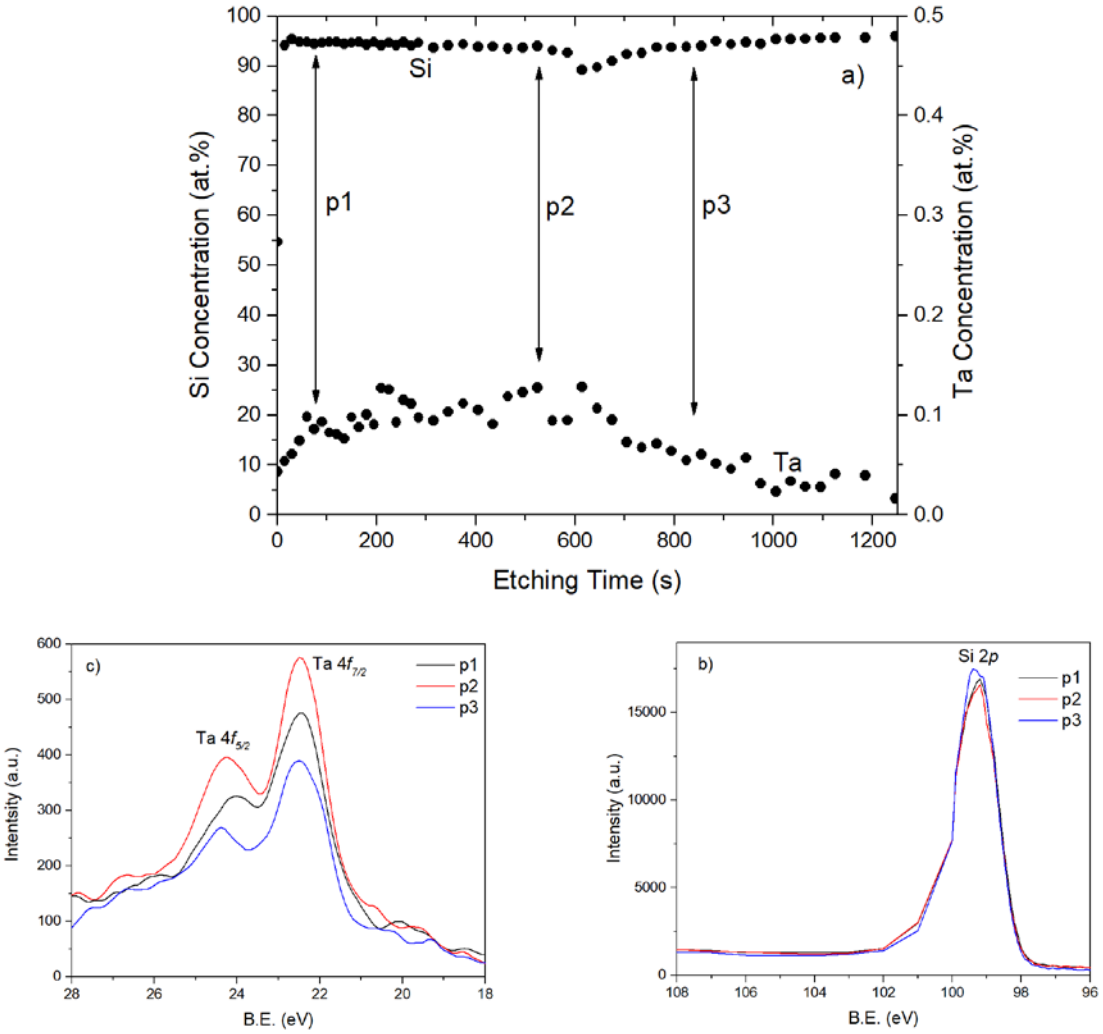

Fig. 4 | Estimation of Ta percentage in Si samples using X-ray photoelectron spectroscopy (XPS). For this purpose, a sample with Si and Ta co-deposited for 60 minutes was prepared in a matrix configuration (thickness corresponding to sample 110^{S}). XPS spectra were acquired with a Kratos AXIS Ultra DLD Photoelectron spectrometer, with an Al Kα (1486.6 eV) source and a base pressure of 10^{-10} mbar. To obtain representative data, XPS measurements were performed at different times of Ar ion etching (ion energy 3 keV). Si and Ta at.% concentrations vs etching times are represented in **a,** estimated from: **b,** *2p* peak for Si and **c)** *4f* for Ta. Si at.% is around 95% while Ta is approximately 0.1%. The difference until sum 100% is O and C (present only in the first measurement). Si oxidation can occur during transportation of the sample from the glovebox to the XPS device.

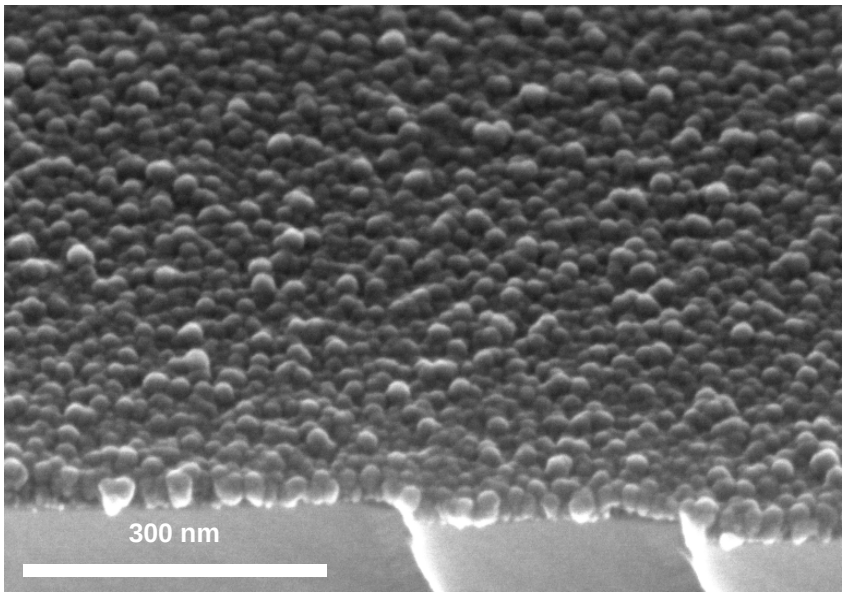

Fig. 5 | Scanning electron microscopy (SEM) cross-section image of sample 25^{C} grown on a Si substrate.

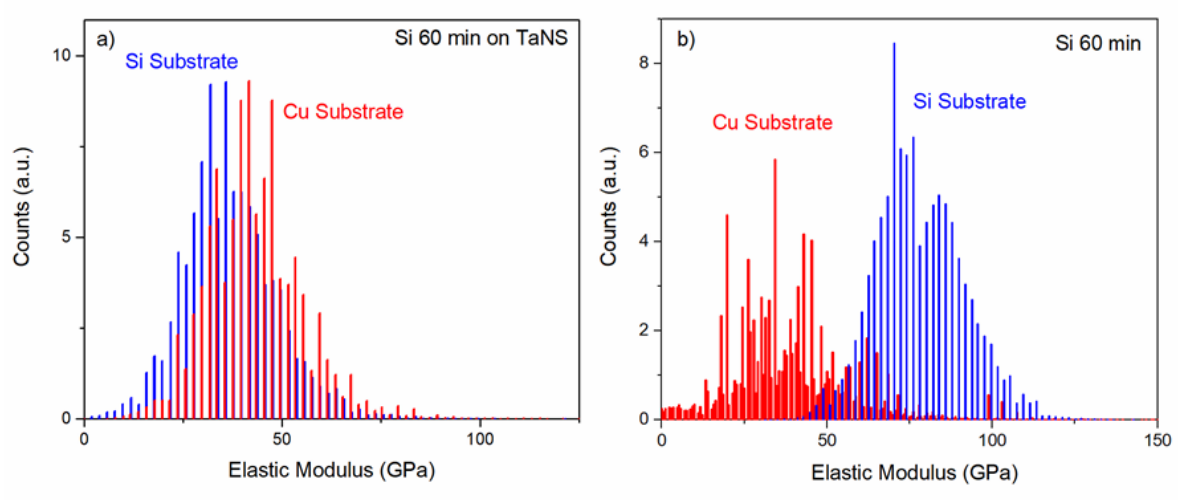

Fig. 6 | Effect of the substrate on elastic modulus measurements. Elastic modulus histogram of **a,** Si sputtered for 60 minutes on the TaNS (sample 110^{S}) and **b,** Si sputtered for 60 minutes directly on the substrate without nanoparticles. *E* of the thin films is independent of the substrate when TaNS is present. Alternatively, *E* strongly depends on the substrate when the deposition is directly on Cu or Si(111). This establishes that, when present, TaNS (and not the substrate) determines the Si growth.

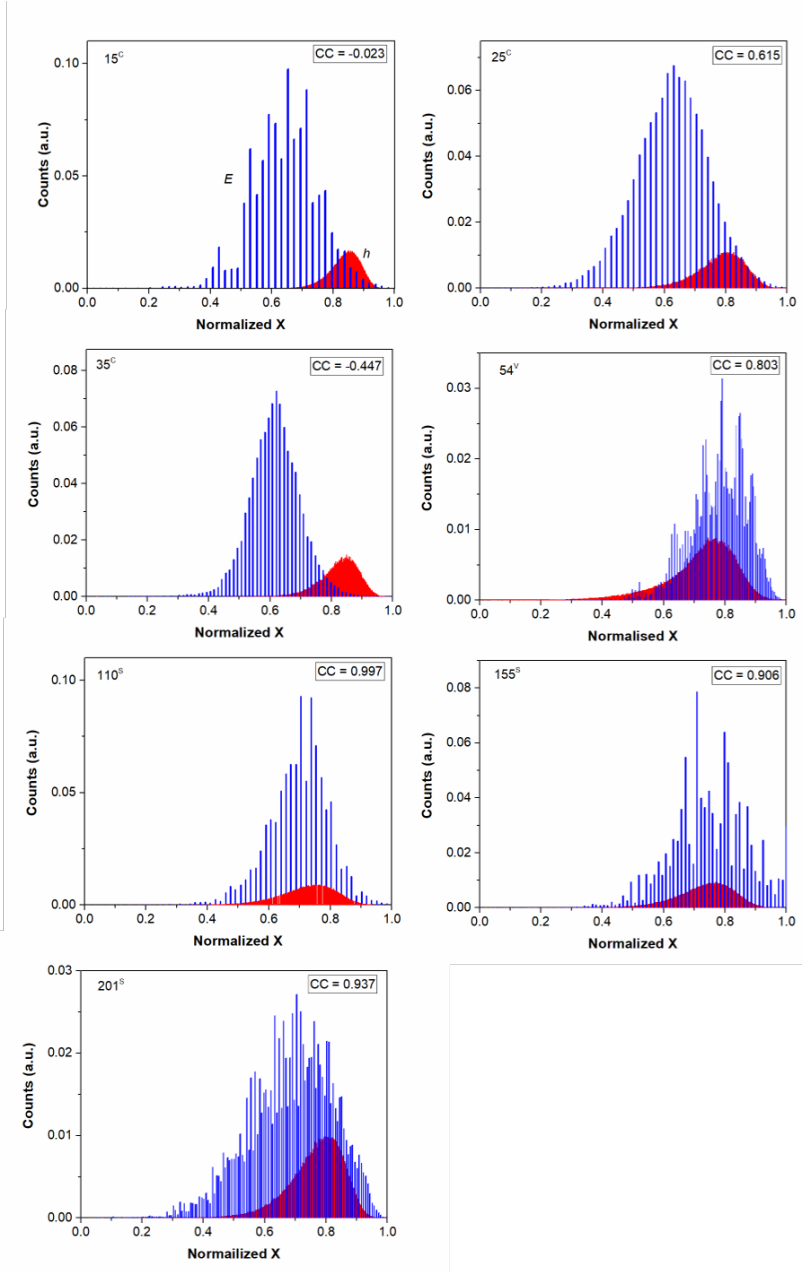

Fig. 7 | Functions of elastic modulus (blue) and height (red) for all samples. The correlation coefficient (CC) is indicated inside each graph. The correlation coefficient of random variances X and Y is a dimensionless measure of a linear relationship of X and Y, defined by:

$$\rho_{X,Y} = \mathrm{cov}(X,Y)/\ \sigma_X\sigma_Y = E[(X-\mu_X)(Y-\mu_Y)]/\sigma_X\sigma_Y \qquad (1)$$

where cov(X, Y) is the covariance of X and Y, μ_X, μ_Y, are the means and σ_X, σ_Y are the standard deviations of variables X and Y respectively, provided that the indicated expectation exists. By dividing the product of the means by the product of the standard deviations, the individual variability of each X and Y is removed. The correlation coefficient is always $-1 \leq \rho \leq 1$. A value of 1 implies that the relationship of X and Y can be described perfectly by a linear equation; thus, as X increases, Y increases too. Accordingly, a value of -1 implies that when X increases, Y decreases. If the correlation coefficient is equal to 0, there is no linear relationship between X and Y.[1]

[1] A.M. Mood, F.A. Graybill, D.C. Boes, Introduction to the theory of Statistics, McGraw-Hill International Editions, **1974**

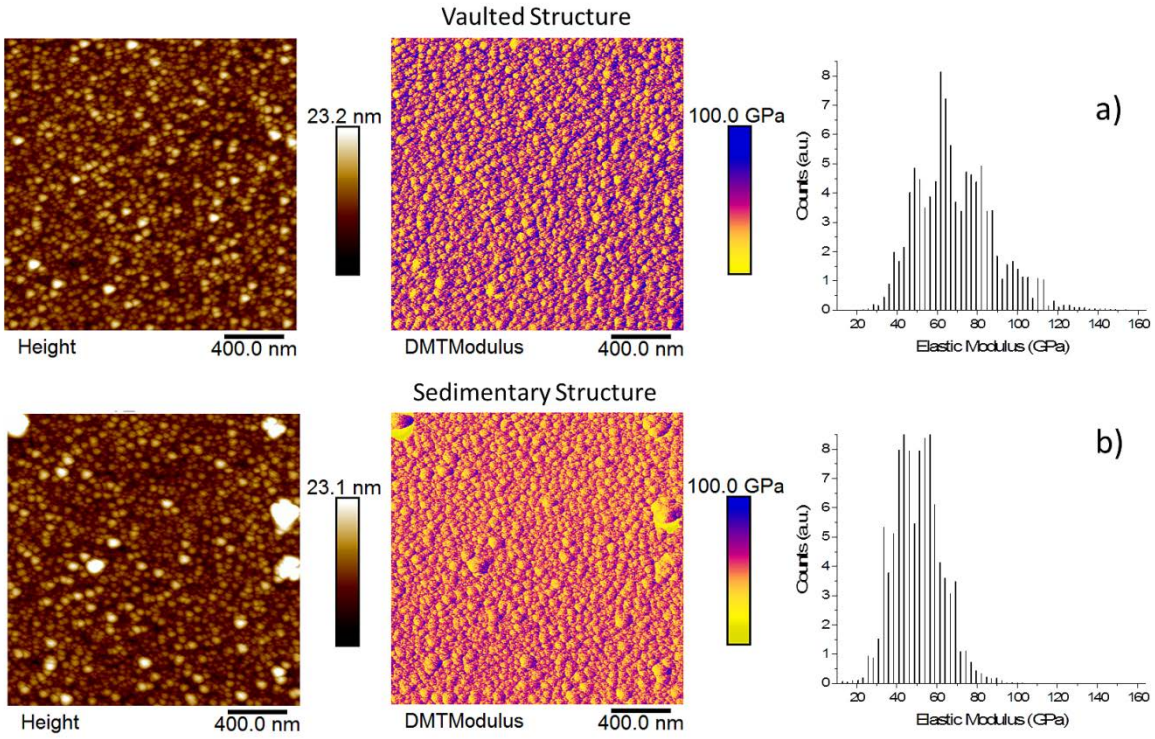

Fig. 8 | Mechanical properties of non-annealed samples measured using PF-QNM. The fabrication process of the samples was identical to those of Fig. 3, save for the omission of step 3, i.e., the thermal annealing stage at 150 ^{o}C for 60 minutes at Ar pressure of 8×10^{-3} mbar. Topography, elastic moduli, and histograms of E for exemplary samples of **a,** vaulted structure (54^{V}) and **b,** sedimentary structure (155^{S}). A significant decrease in E values can be observed for the former (i.e., an average of ~ 60-70 GPa) compared to an average of ~ 120 GPa for annealed samples. In contrast, there was no discernible effect of the annealing treatment (or the lack of) to the latter, which showed an average value of ~ 40-50 GPa, similar to those of the annealed samples. This control experiment confirms the importance of thermal annealing for the strengthening of the vaulted structure through the mobilisation and ensuing eradication of voids, leading towards more rigid individual columns.

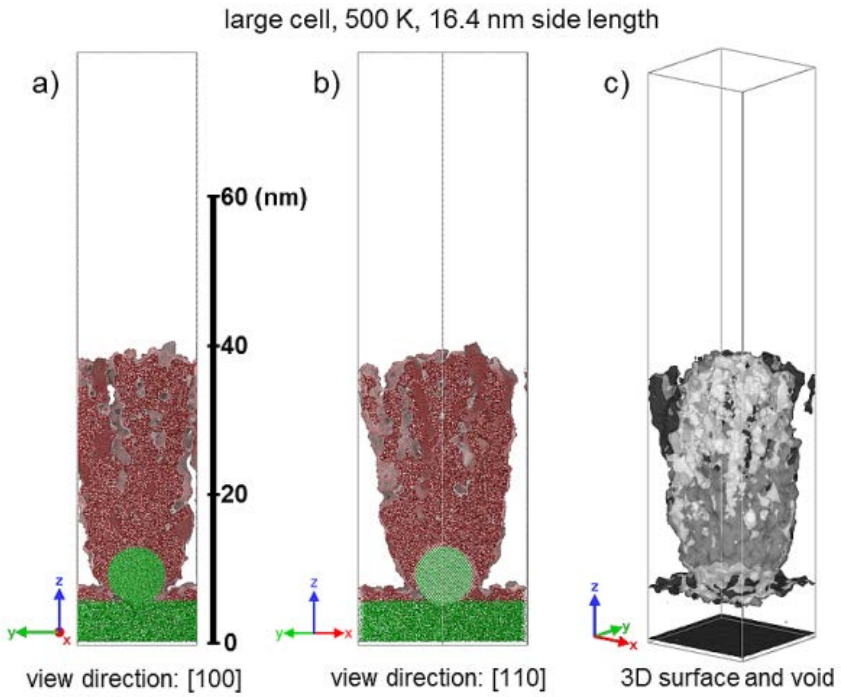

Fig. 9 | Si deposition on a single nanoparticle. Both the simulation box and the nanoparticle are larger than that of Fig. 4 (i.e., 16.4 nm in side length and 8 nm in diameter, respectively) to explicitly study the size effect. Other than that, the setup is identical to that of Fig. 4 (i.e. the simulation box is duplicated along the (100) direction, due to periodic boundary conditions, and the temperature is 500 K). Once again, the Si film follows columnar growth and forms a vaulted structure. The simulation box is sliced for clear observation, viewed along **a,** the (100), and **b,** the (110) direction. **c,** The right panel depicts the surface mesh inside the deposited layer (i.e., without the atoms) in 3D, indicating the presence of voids.

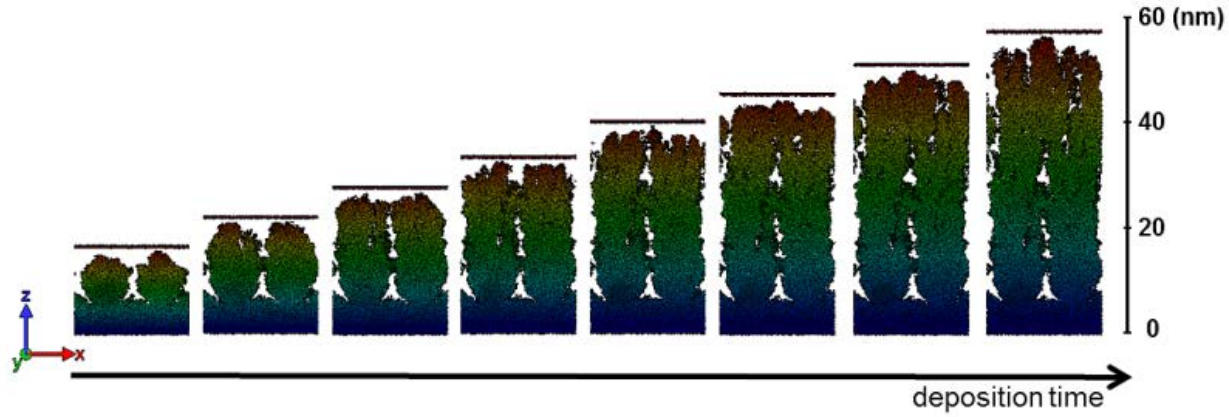

Fig. 10 | Si deposited on two neighbouring nanoparticles. Two nanoparticles were explicitly introduced in a simulation box twice as long in this simulation group, to avoid the symmetry present in simulations represented by Fig. 4. Other than that, the setup is identical to that of Fig. 4 (i.e., the simulation box is duplicated along the (100) direction, due to periodic boundary conditions, and the temperature is 500 K). Once again, the Si film follows columnar growth and eventually forms a vaulted and a sedimentary structure. The simulation box is sliced for clear observation, viewed along the (100) direction. Snapshots are taken from Supplementary Movie 2, where the evolution of growth can be assessed clearly.

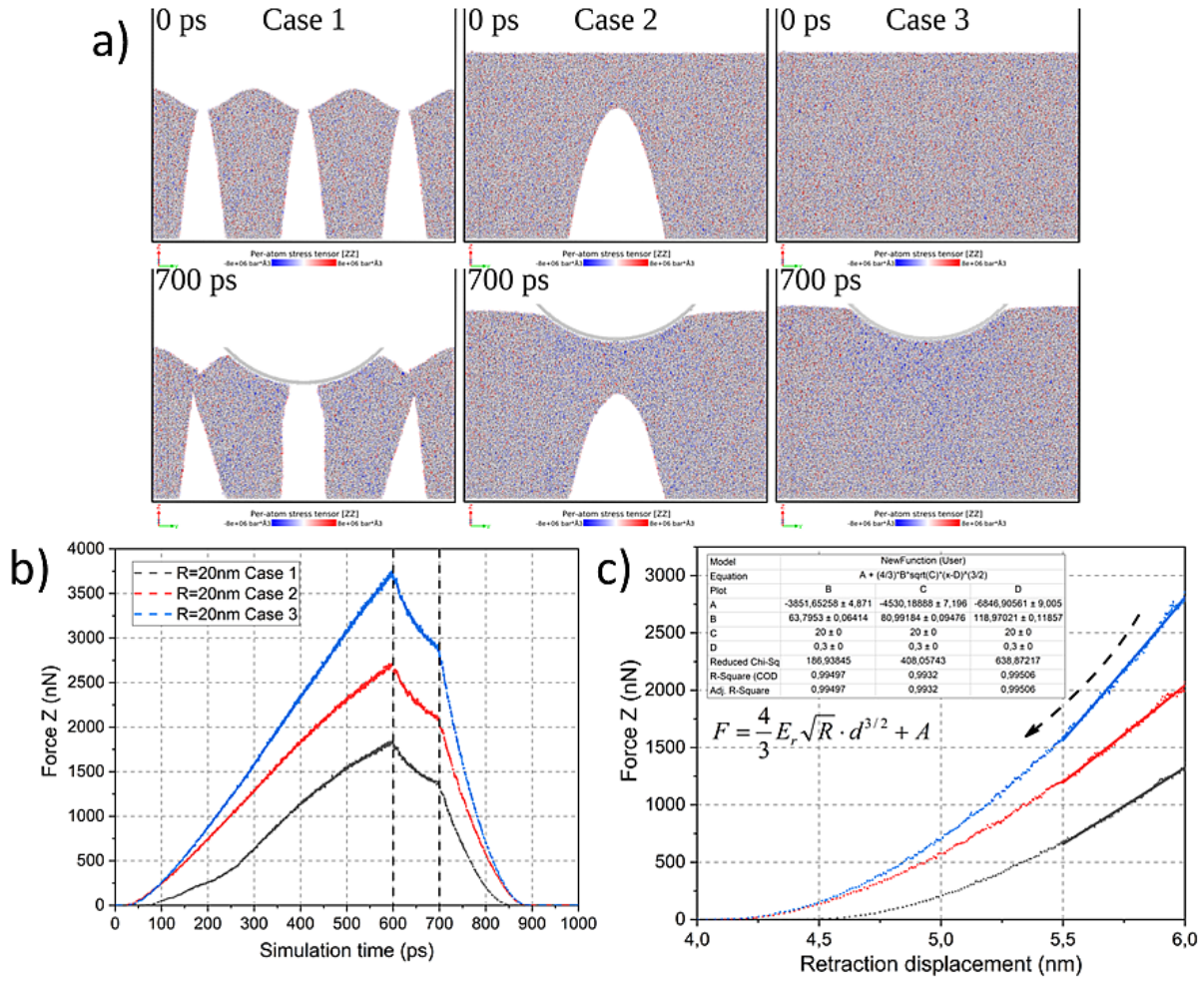

Fig. 11 | Effect of density on elastic properties. a, Snapshots of nanoindentation MD simulations on samples pre-cut from bulk a-Si (standard a-Si density at 300 K: 4.90×10^{22} atom/cm^3, or 2.285 g/cm^3). The columnar (case 1) and vaulted (case 2) samples were constructed from the relaxed bulk a-Si sample (case 3) by removing atoms in the defined regions and then relaxed for 50 ps at room temperature. The size of the rigid indenter tip was 20 nm in radius. **b,** Evolution of the feedback forces along compress-hold-decompress loops. The nanoindentation simulations were performed with an indentation rate of 0.1 Å/ps and hold duration of 100 ps. **c,** The reduced elastic moduli, E_r, can be fitted from the retraction force curves as functions of the displacements. Derived values were 63.8, 81.0, and 119.0 GPa for columnar, vaulted and bulk samples, respectively. Clearly, a bulk a-Si sample similar in density with the pillars of the columnar and vaulted structure (i.e., lacking the additional porosity observed in sedimentary structures) is stiffer than both latter structures, indicating the effect of sample density on the elastic properties.

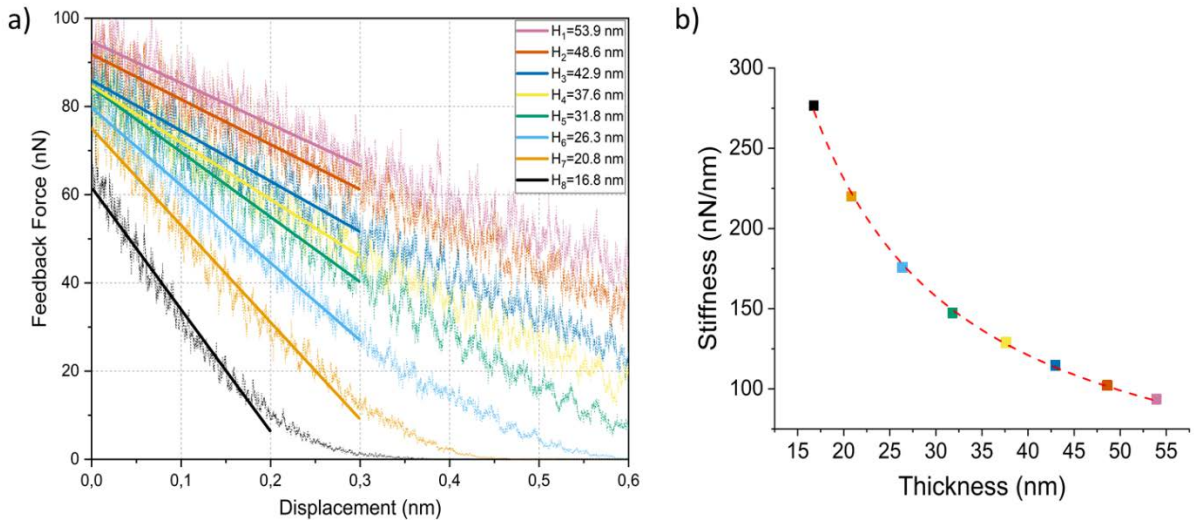

Fig. 12 | Elastic deformation during the unloading process. a, The stiffness of the corresponding structures, as shown in Fig.4c, is extracted from the slopes of the linear fitting lines of the curves (solid lines). **b,** The decompression stiffness as a function of structure thickness drops in a monotonous fashion, unlike that during the loading process. The red dashed curve shows the non-linear fitting from Eq. 2, below.

Validation of the porosity value provided by MD:

The porosity of the deposited amorphous silicon structure is strongly affected by the sputtering conditions and temperature, as such parameters determine adatom mobility.[2] The porosity obtained through our MD simulations can be estimated by comparing the number density of Si atoms in a porous structure whose volume can be measured from the surface construction analysis, with a reference number density for a bulk amorphous silicon sample. Such analysis resulted in a porosity value of ~ 0.3.

In the elastic regime, the deposited structure can be approximated by a spring, the stiffness of which is inversely proportional to the length:

$$S = AE/L, \qquad (2)$$

where A is the cross-section area, E is the modulus of elasticity, and L is the length. For this structure, the cross-section area A is 10.89 nm × 10.89 nm. The relation between the modulus of elasticity and the porosity was studied extensively. The estimation is

$$E = E_0(1-p)^2, \qquad (3)$$

where p is the porosity; therefore, from the unloading stiffness, we can calculate the bulk Young's modulus E_0 as 75 GPa, which is in good agreement with the literature value,[3] thus validating our method.

[2] A. Lakhtakia & R. Messier, Sculptured thin films: nanoengineered morphology and optics. SPIE Press, Bellingham, WA, USA, **2005**

[3] L.B. Freund & S. Suresh, Thin film materials: stress, defect formation and surface evolution. Cambridge University Press, page 104, **2004**

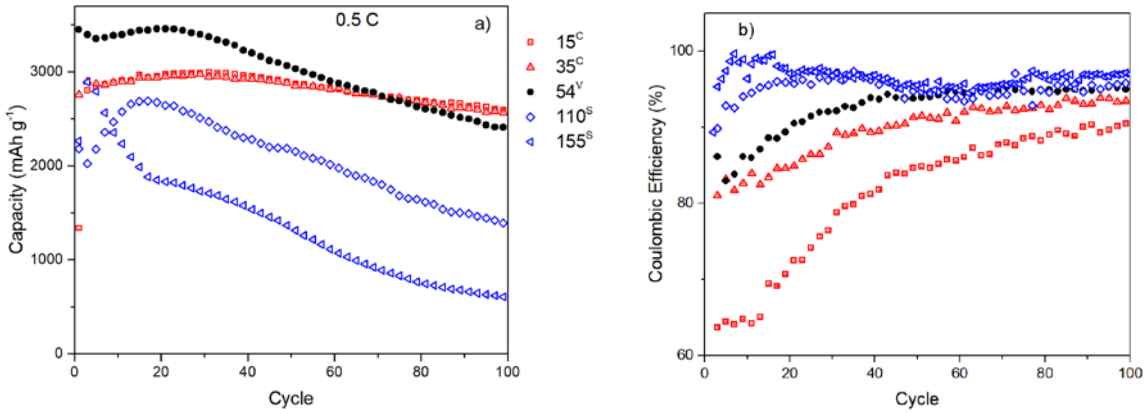

Fig. 13 | LIB performance of Si samples showing different behaviours according to the structure and *E* characteristics. a, charge capacity (Si electrode delithiation) and **b,** Coulombic efficiency.

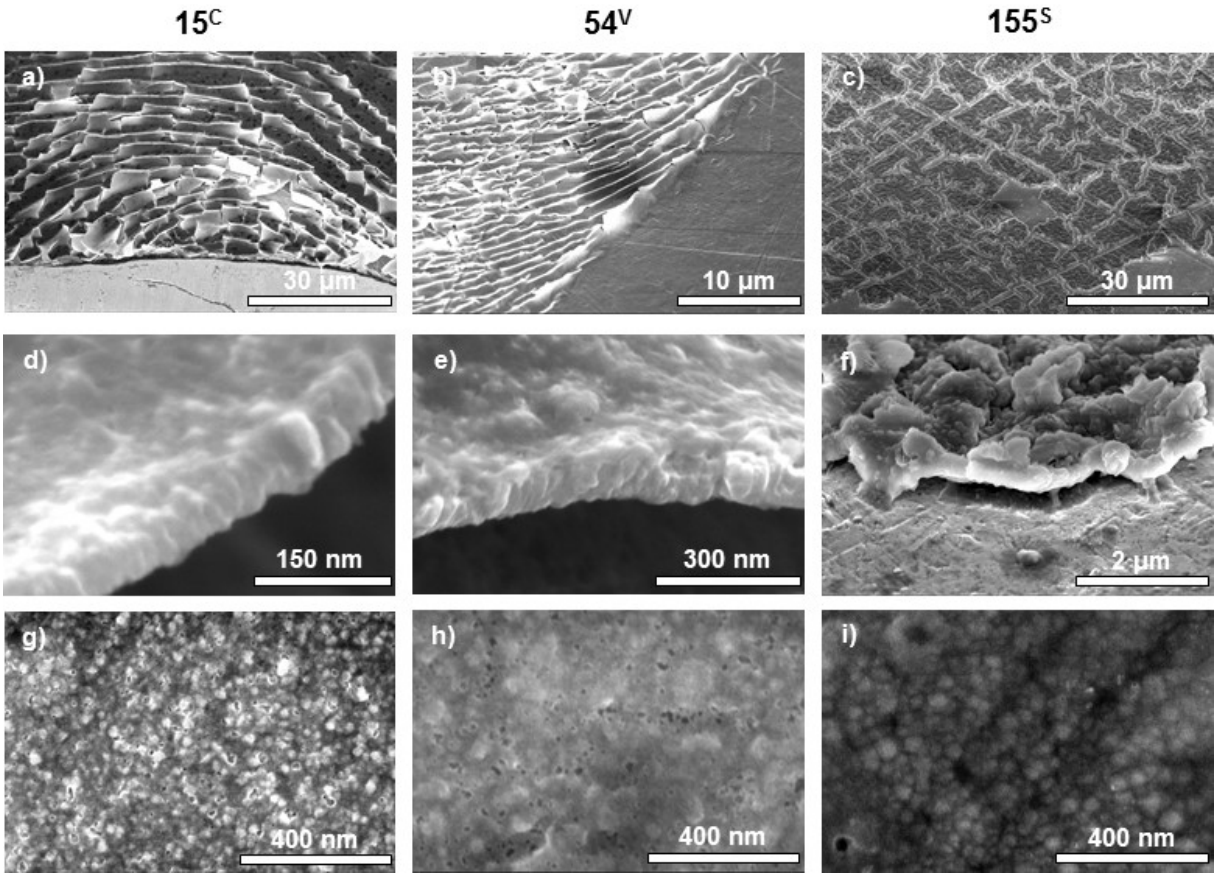

Fig. 14 | SEM images of samples 15^{C} (a, d, g), 54^{V} (b, e, h), and 155^{S} (c, f, i) after three charge-discharge cycles at 0.5 C between 0.01 and a 1 V. Imaging the physical condition of electrodes after cycling can help explain their electrochemical behaviour. Once the electrodes were delithiated, the semibatteries were opened inside the Ar glovebox and the anodes cleaned with dimethyl carbonate and dried in high vacuum. Low magnification images (first row) show the ripples formed on 15^{C} and 54^{V} by a diamond pen scratch; similar scratching was not necessary for sample 155^{S}, which shows a highly cracked film forming islands. Cross-sections (second row) show the columnar and vaulted structure at the edge of the ripples, and a detached film at the edge of the cracked island for sample 155^{S}. This can attribute the high Coulombic efficiency concurrent with the high capacity fade observed for 155^{S}, not to exposure of fresh electrode to electrolyte, but, instead, to loss of active material. Top-down, high-magnification images of the cycled anodes (third row) show the formation of holes. The holes are especially prevalent in the 15^{C} and 54^{V} structures, and can be attributed to channels created by the electrolyte during cycling, most likely associated with the activation phenomenon (during activation more active material is involved in the lithiation process during cycling).

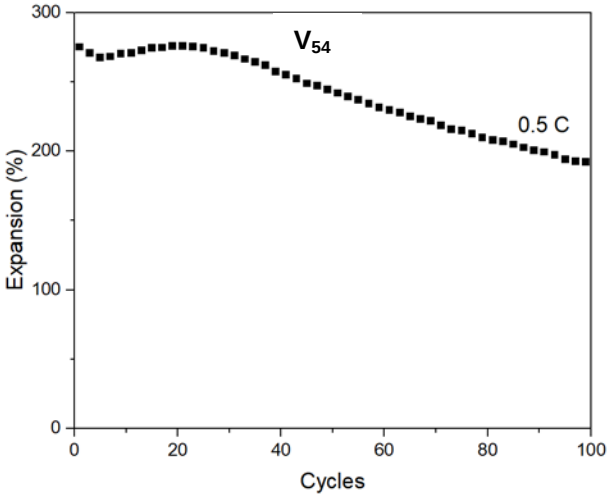

Fig. 15 | Volume expansion of the electrode 54^{V} in a lithium semibattery at 0.5 C, estimated according to V. L. Chevrier et al.[4]

[4] V.L. Chevrier, L. Liu, D.B. Le, J. Lund, B. Molla, K. Reimer, L.J. Krause, L.D. Jensen, E. Figgemeier, K.W. Eberman *J. Electrochem. Soc.* **2014**, 161, A783

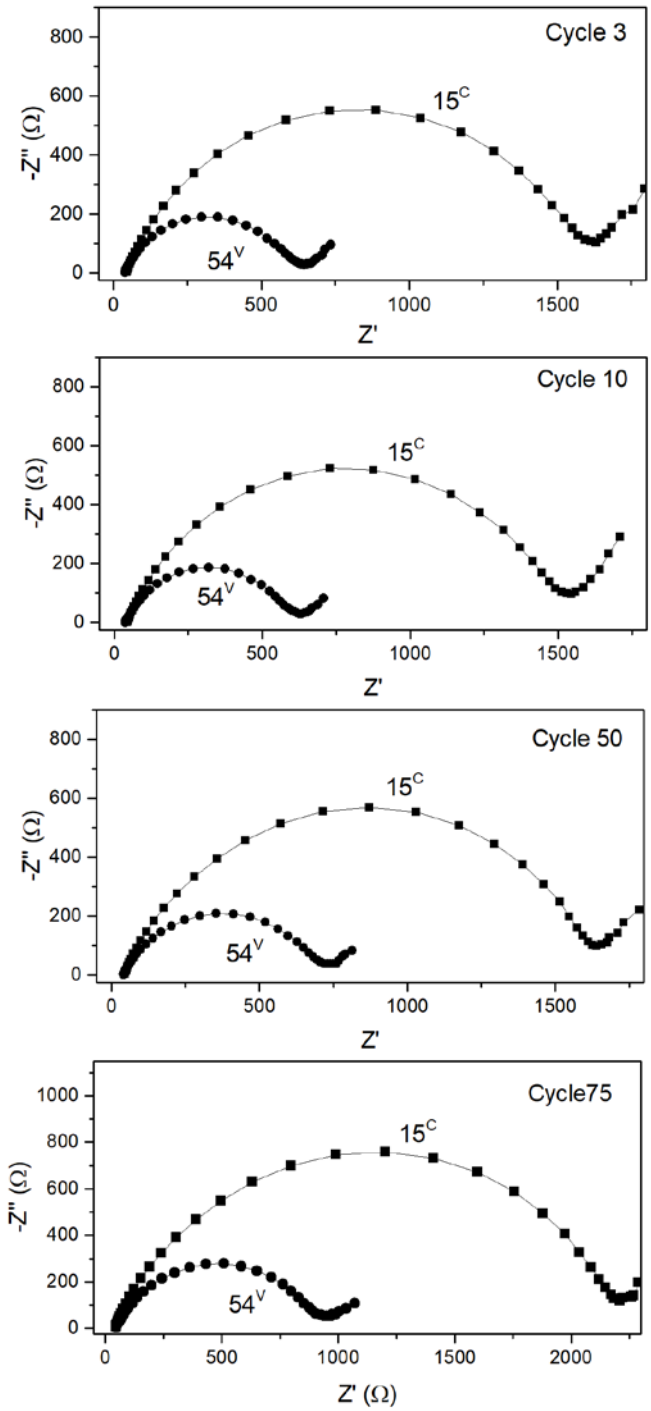

Fig. 16 | Nyquist plots of 54^{V} and 15^{C} registered at an open circuit after several cycles, indicated inside the figure. The resistance at high frequency is associated with the electrode/electrolyte interfacial resistance (SEI and the charge transfer),[5] and it is three times higher for 15^{C} than for the 54^{V} sample. This confirms that the higher electrode/electrolyte interface in the columnar structure is responsible for the larger SEI.

[5] N. Vicente, M. Haro, G. Garcia-Belmonte *Chem. Commun.* **2018**, 54, 1025

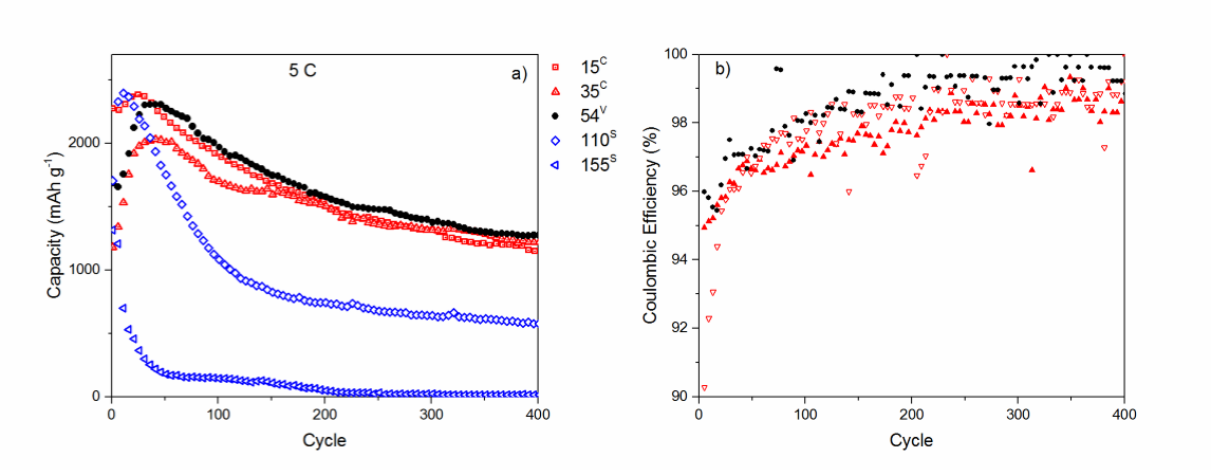

Fig. 17 | LIB performance of Si samples showing different behaviours according to the structure and *E* characteristics. a, Charge capacity (Si electrode delithiation) and **b,** Coulombic efficiency. The values are close to 100%, but they are not significant because the capacity fade suggests the sample becomes fractured.

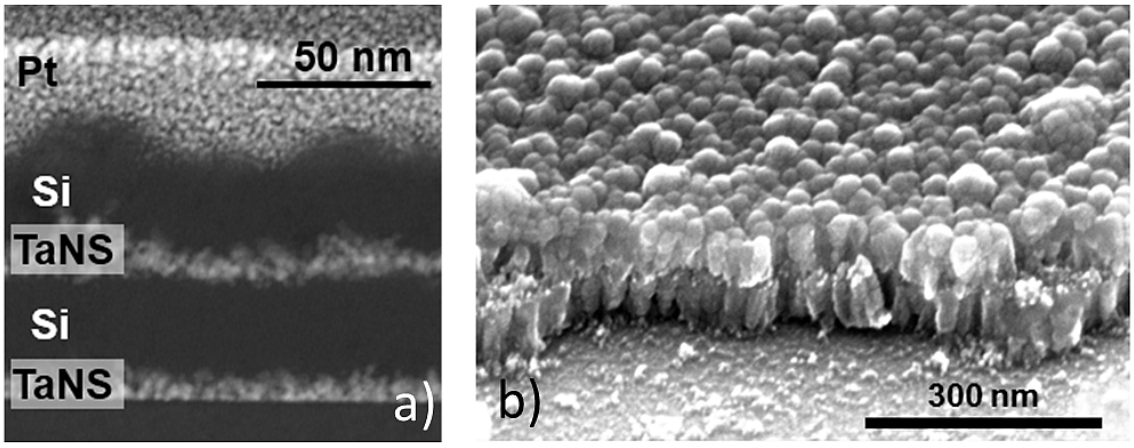

Fig. 18 | Characterisation of D54^{V} sample grown on Si substrate before lithiation-delithiation cycling. a, TEM lamella image, **b,** SEM image. A double-vaulted structure is evident instead of a sedimentary structure fabricated with the same amount of Si and a single TaNS (110^{S}).

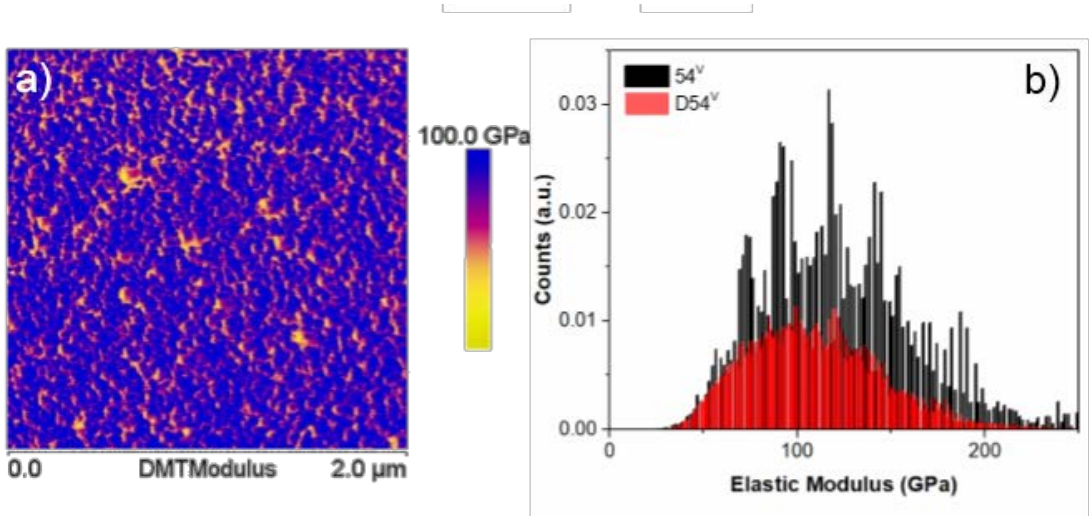

Fig. 19 | Mechanical properties measured using PF-QNM of the D54^{V} sample. a, Elastic modulus (most of the mapping is saturated because the scale is the same as the scale used in Fig. 3), and **b,** corresponding histogram. The histogram shows a comparison between the D54^{V} and 54^{V} samples.

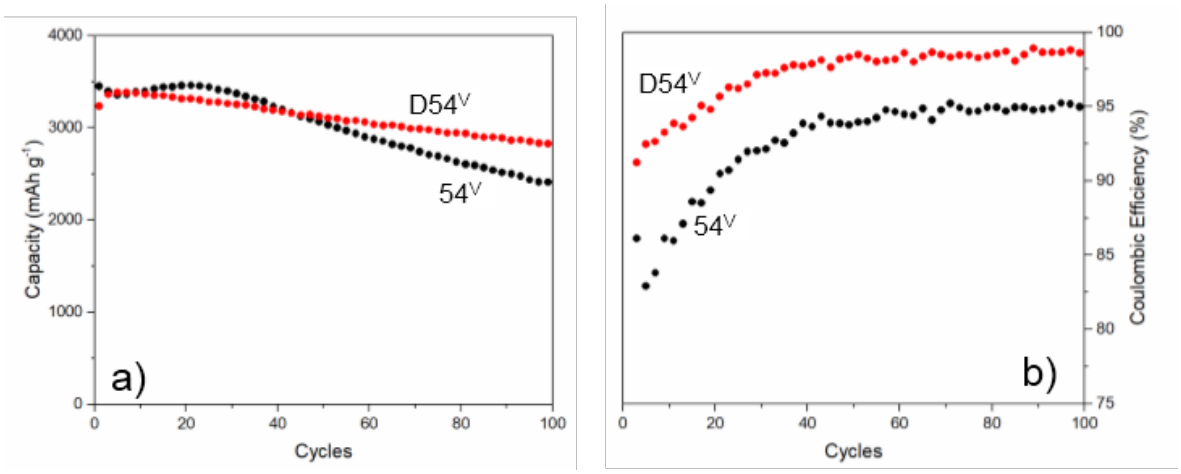

Fig. 20 | a, Charge (delithiation) capacity and b, Coulombic efficiency of LIB semibatteries cycled at 0.5 C for $D54^V$ and 54^V samples.

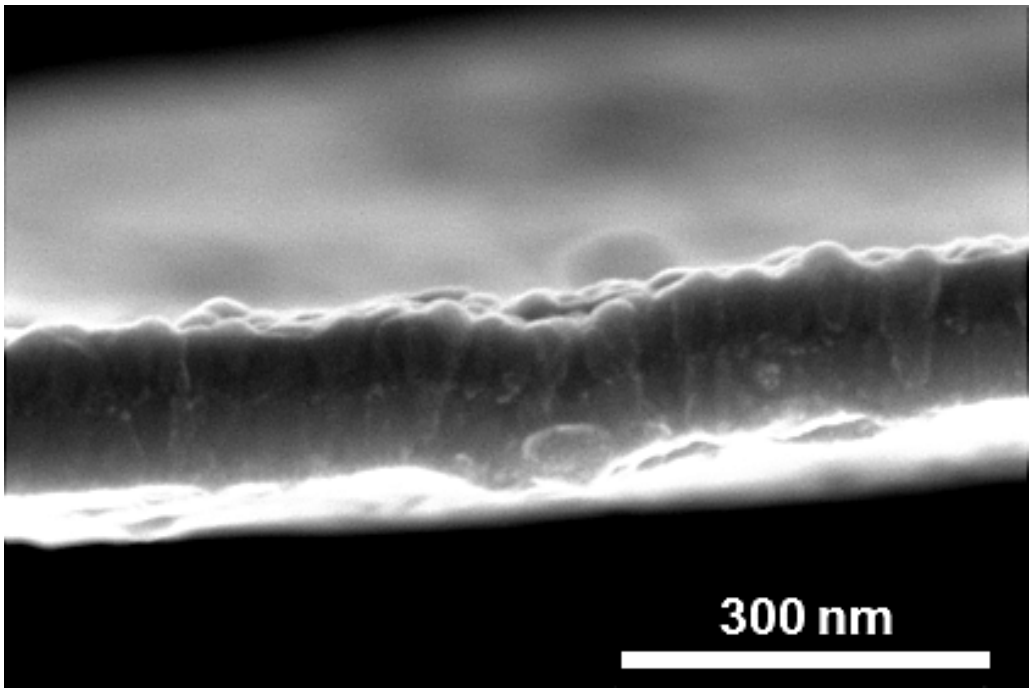

Fig. 21 | SEM image of sample D54^{V} after three lithiation-delithiation cycles. The sample was grown on a Cu foil so that the anode could work in a semibattery. The bilayer structure is retained after charge-discharge cycling.